PAPER

Facile synthesis of FeS–Fe₃O₄ nanocomposites: highly stable & enhanced electrochemical performance in asymmetric supercapacitor applications

Junaid Riaz, [ID] [a] Zahra Bayhan,[b] Ghulam Murtaza,[c] Muhammad Arif*[a] and Amina Bibi*[d]

Over the last decade, researchers have required electrode materials that have higher energy density and are highly stable to make the next generation of supercapacitors. This study developed and analyzed a FeS–Fe₃O₄ nanocomposite as a potential positive electrode material for asymmetric supercapacitors. Structural and morphological analyses were performed using XRD and FESEM, with EDX and EDS mapping. The FeS–Fe₃O₄ composite worked better than both pure FeS and pure Fe₃O₄ when tested with a 3 M KOH electrolyte. At 1 A g⁻¹, it has a specific capacitance of 464.6 F g⁻¹, and at 4 A g⁻¹, it has a specific capacitance of 186.9 F g⁻¹. The better performance is because FeS conducts electricity better, and Fe₃O₄ acts like a pseudocapacitor. These two factors work together to speed up the movement of ions and the redox processes. The supercapacitor fabricated in this work exhibits a unique configuration that has never been reported before. The negative electrode was made of activated carbon, and the positive electrode was made of FeS–Fe₃O₄. It can work within a voltage window of 1.4 V. The device had a power density of 699.6 W kg⁻¹ and an energy density of 46.10 Wh kg⁻¹. It also delivered a high power density of 3998.4 W kg⁻¹, with a low energy density of 30.17 Wh kg⁻¹. After 12 000 charge–discharge cycles, the device retained 98.6% of its capacitance and about 99.8% coulombic efficiency, which indicates good cycling stability. The results show that the FeS–Fe₃O₄ nanocomposite is a very good electrode material for energy storage systems that need to be stable and work well.

1. Introduction

In the last few decades, industrialization and fast economic growth have caused excessive use of fossil fuels, which has played a big role in global warming.[1–4] It is important to create energy technologies that are both long-lasting and affordable as society moves into the next phase in order to meet the needs of modern living and industry. The rising demands of manufacturing, mechanization and the global economy are driving an increase in energy demand.[5–8] This increased demand for renewable energy sources is vital for preserving global ecosystems. Without the use of renewable energy, it will be impossible to halt the depletion of the ozone layer.[9–12] Developing a clean, safe, and efficient system for energy conversion and storage is crucial. Supercapacitors show great potential in addressing the energy storage requirements of electronic devices, including hybrid and electric vehicles (EVs and HEVs). Their fast charging ability, high power density, and long cycle life make them ideal for applications that require rapid energy release. Their versatility in supplementing or replacing batteries in certain situations further enhances their value in the development of advanced energy storage technologies.[13–19] Supercapacitors are superior to conventional capacitors because they can store more energy, work in a wider range of temperatures, and have a higher specific capacitance. The capacitance in supercapacitors increases due to the inter-action between the electrolyte and the electrode material on nickel foam, or it can arise from the faradaic electron charge generated during redox reactions or intercalation processes. Faradaic reactions make charge transfer easier.[20] A lot of researchers are interested in hybrid supercapacitors (HSCs) since they perform very well when electric double-layer capaci-tors (EDLCs) and pseudo-capacitors (PCs) are coupled. The electrochemical characteristics and capacitance are enhanced

aYunnan Key Laboratory of Optoelectronic Information Technology, School of Physics and Electronic Information, Yunnan Normal University, Kunming 650500, China. E-mail: junaidriaz1990@gmail.com

bDepartment of Physics, College of Sciences, Princess Nourah bint Abdulrahman University, P.O. Box 84428, Riyadh 11671, Saudi Arabia

cSchool of Ecology and Environmental Science, Yunnan University, Biocontrol Engineering Research Center of Crop Diseases & Pests, Kunming 650500, Yunnan Province, China

dDepartment of Physics, Hazara University, Mansehra 21300, Pakistan. E-mail: aminaamni11@gmail.com

when faradaic redox processes are combined with double layers.[21–23] The type of material used for the electrode has a huge effect on how well HSCs perform, similar to batteries. This is because the energy density, power density, and cycle stability are affected.[24–26] Electric double-layer capacitors (EDLCs) store charge through ion adsorption at the electrode–electrolyte interface, typically using carbon-based materials, offering high power density and long-term cycling stability. In contrast, pseudocapacitors (PCs) store energy *via* fast faradaic redox reactions in electroactive materials such as metal oxides or conducting polymers, providing higher capacitance. Hybrid supercapacitors combine EDLC and pseudocapacitive electrodes to achieve improved energy density and rate capability.[27–29] Because of these qualities, metal sulfides and other metal compounds, such as metal oxides, are thought to be some of the best materials for electrodes in the next generation of supercapacitors.[30]

Transition metal oxides (TMOs), such as ZnO, Fe_2O_3, NiO, $CoAl_2O_4$ and Fe_3O_4, have been widely researched as effective electrode materials for supercapacitors, offering higher capacitance than conventional electric double-layer capacitors (EDLCs).[31–35] These TMOs utilize redox reactions to provide superior specific energy compared to traditional carbon-based materials, and they also show greater durability than conducting polymers.[36–38] Iron oxides are well known for their excellent electrochemical redox characteristics, high capacity, environmental friendliness, abundance, non-toxicity, and low cost.[39] Iron oxides can store charge across a wide voltage range because Fe^{3+} and Fe^{2+} can undergo reversible oxidation and reduction. However, iron oxides, specifically Fe_3O_4, have relatively low conductivity and stability, which limits their electrochemical performance and cycling stability.[40]

Magnetite (Fe_3O_4) is one of the transition metal oxides that has been found to have excellent conductivity and high electrochemical activity. This substance is appealing since it is abundant in nature, safe for people and the environment, and has little effect on the environment.[41] Wang *et al.* examined the electrochemical performance of Fe_3O_4 nanoparticles exhibiting a high surface area (165.05 m^2 g^{-1}) produced *via* a hydrothermal process.[42] Reyes *et al.* created Fe_3O_4 nanoparticles that have a specific capacitance of 36 F g^{-1}.[43] The specific capacitance of Fe_3O_4 is still lower than that of other transition metal oxides, though. Iron oxides are particularly important among transition metal oxides because of their environmental sustainability and abundant natural reservoirs, along with intrinsic pseudocapacity properties, making them an outstanding choice for faradaic pseudo-capacitors. Insufficient electrical conductivity and particle agglomeration during charge/discharge cycles, on the other hand, limit Fe_3O_4, causing a sharp drop in capacity at elevated current densities and following extended cycling.[44–48] Chang *et al.*[49] prepared Fe_3O_4/graphene nanocomposites through a solvothermal process and obtained a specific capacitance of 300 F g^{-1} at 0.4 A g^{-1}. Regardless of such improvements, there are still limitations to the practical application of Fe_3O_4-based materials including short cycle life, rate capability, and low electrical conductivity that impede their large-scale utilization.[50] Iron sulfide (FeS) meets all the important requirements for supercapacitor electrode materials, such as being cheap, plentiful, and non-toxic. In the last few decades, many people have worked on making FeS nanosheets so that they can take advantage of these benefits. It is very important to make new electrode materials like FeS since they are in great demand and cheap, and have a large surface area. These factors are important for making supercapacitor technology more commercially viable.[51]

This study focuses on the development of hybrid electrode materials that effectively combine high electrical conductivity with significant redox activity, suggesting a promising yet complex strategy to improve supercapacitor performance. TMS and TMO have attracted significant interest due to their synergistic electrochemical capabilities; yet, their specific restrictions often hinder practical applications. To address these challenges, this study demonstrates the systematic fabrication of a FeS–Fe_3O_4 nanocomposite, in which the synergistic interaction between conductive FeS and pseudocapacitive Fe_3O_4 markedly enhances charge storage performance. The FeS–Fe_3O_4 nanocomposite has a high specific capacitance of 464.6 F g^{-1} at 1 A g^{-1} and preserves its outstanding rate capability because its porous structure is well-integrated. When used to create an asymmetric supercapacitor using activated carbon as the negative electrode, the device operates over a broad voltage range of 1.4 V. It has a high energy density of 46.10 Wh kg^{-1} and can retain 98.6% of its capacitance after 12 000 charge–discharge cycles, which indicates good cycling stability. These results demonstrate that FeS–Fe_3O_4 nanocomposites could be highly beneficial as electrode materials and represent an excellent approach to develop energy storage devices that perform well and have long-term stability.

2. Experimental section

2.1 Materials for experiments

All materials were purchased from Sigma-Aldrich (China) and used in the experiments without further treatment or purification: ferrous sulfate heptahydrate ($FeSO_4 \cdot 7H_2O$), iron(III) chloride hexahydrate ($FeCl_3 \cdot 6H_2O$), thioacetamide (C_2H_5NS), ammonia solution ($NH_3 \cdot H_2O$), sodium hydroxide (NaOH), ethanol (C_2H_5OH), hydrochloric acid (HCl), *N*-methyl-2-pyrrolidone (NMP), polyvinylidene (PVDF), acetone and DI water.

2.2 Hydrothermal synthesis of Fe_3O_4

To prepare Fe_3O_4 by using the hydrothermal method, 0.1 mmol solution of ferrous sulfate ($FeSO_4 \cdot 7H_2O$) was added to 40 ml DI water. The mixture was placed on a hotplate stirrer for 3 h at room temperature. The pH of the solution was maintained at 10 by adding ammonia solution dropwise into the solution during heating at 80 °C for 40 min, due to which the color of the solution changed from bright green to black. Then the solution was transferred into an autoclave and put into a furnace at 80 °C for 4 h. After cooling naturally to room temperature, the particles were washed by centrifugation at 4000 rpm until their pH reached 7. After washing the sample many times, the sample

was put into an oven for drying at 60 °C overnight to remove the water residue.

2.3 Hydrothermal synthesis of FeS

For the preparation of FeS, 6.8 g of C_2H_5NS and 5.8 g of $FeCl_3 \cdot 6H_2O$ were dissolved under magnetic stirring in 15 ml of DI water and 5 ml of ethanol. After 30 minutes of magnetic stirring at room temperature, the beaker was subjected to ultrasonic treatment for the next 40 minutes for homogenous mixing. Then the prepared solution was transferred to a 30 ml stainless autoclave and heat-treated for the next 2 h at 150 °C. The thermal treatment in the autoclave facilitates good crystallinity and the desired morphology. After cooling to room temperature in an open atmosphere, the sample was washed by centrifuging many times and then put into an oven at 70 °C for the next 4 h.

2.4 Preparation of FeS–Fe₃O₄ composites

For the preparation of FeS–Fe₃O₄ composites *via* wet chemical method, we take the weight ratio of our prepared samples, FeS, and Fe₃O₄, and dissolved them in 20 ml of DI water by adding sodium hydroxide using a magnetic stirrer, at 60 °C for 2 h. After that, we provide the ultrasonic treatment for 40 minutes to disperse our materials. And then put into the oven for drying at 80 °C overnight, and get the FeS–Fe₃O₄ composite with enhanced electrochemical performance, then pure FeS, and Fe₃O₄ materials.

2.5 Electrode preparation process

For the preparation of Fe₃O₄, FeS, and FeS–Fe₃O₄ composite electrodes, first, we cut the Ni-foam into a 1 × 1 cm circular shape, washed it with acetone, 3 M HCl, 100% ethanol, and DI water several times, and dried it by putting it into an oven and measured its mass. Then we made slurry by using 80% active material (Fe₃O₄, FeS, or FeS–Fe₃O₄ composite), 10% activated

carbon (AC), and 10% polyvinylidene (PVDF) by adding *N*-methyl-2-pyrrolidone (NMP) drop-wise. Then, this slurry was coated onto the Ni-foam substrate and dried in an oven for 12 h at 60 °C. To further enhance the conductivity of the porous Ni-foam, the prepared electrode was pressed under a pressure of 100 kPa for 2 min. The mass of the active material was determined by measuring the difference in weight of the Ni-foam substrate before and after electrode fabrication (for details see Fig. 1).

2.6 Characterization

The successful synthesis of Fe₃O₄, FeS, and FeS–Fe₃O₄ composites was confirmed by X-ray diffraction (XRD) analysis using a Donghua TD-3500 diffract meter over a 2θ range of 20°–70°. The morphology of the samples was examined *via* Field Emission Scanning Electron Microscopy (FESEM) using a JEOL JSM-7800F instrument. The electrochemical performance, cyclic voltammetry (CV), galvanostatic charge discharge (GCD), and EIS, of the prepared electrodes was evaluated in a 3 M KOH aqueous electrolyte using a Donghua DH7000C workstation. A platinum wire and an Ag/AgCl electrode were employed as the counter and reference electrodes, respectively. After that an asymmetric supercapacitor were fabricated and its electrochemical performance was evaluated using FeS–Fe₃O₄ as the positive electrode and activated carbon (AC) as the negative electrode in 3 M KOH electrolyte and its stability was tested at 1.4 V over 12 000 charge–discharge cycles. Furthermore all other electrochemical parameters were calculated by using these equations.

$$C_s = \frac{I \times \Delta t}{m \times \Delta V} \tag{1}$$
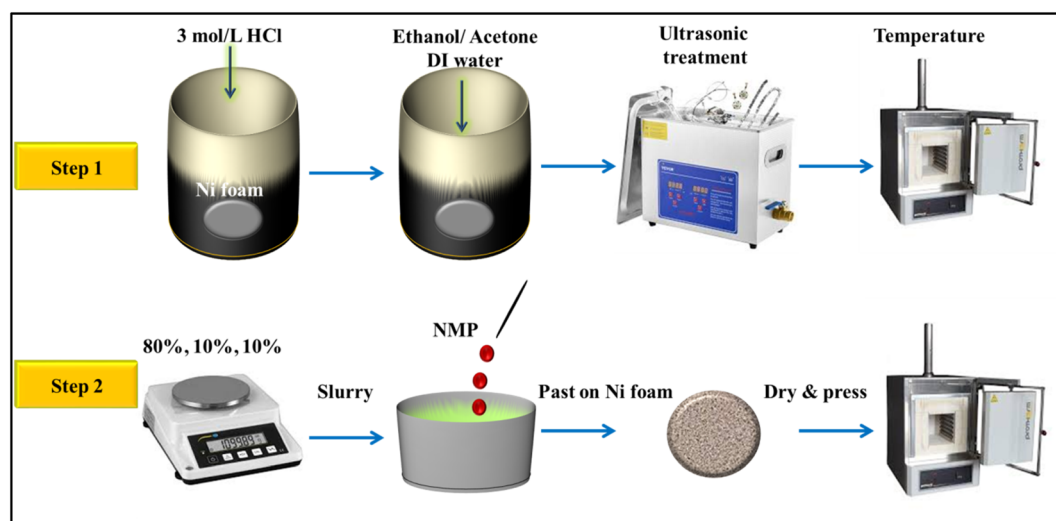
$$E = \frac{C_s \times \Delta V^2}{7.2} \tag{2}$$

Fig. 1 Preparation method for FeS, Fe₃O₄, and Fes−Fe₃O₄ composite electrodes.

$$P = \frac{3600 \times E}{\Delta t} \tag{3}$$

$$\eta = \frac{T_d}{T_c} \times 100\% \tag{4}$$

where C_s (F g^{-1}) denotes the specific capacitance, I/m signifies the current density, ΔV represents the potential difference, Δt indicates the discharge duration, and E (Wh kg^{-1}) and P (W kg^{-1}) correspond to energy and power density, respectively.

3. Results and discussion

3.1 Elemental analysis of prepared samples

The diffraction peaks of Fe_3O_4 matched with JCPDS # 01-074-33 showing peaks at positions 30°, 35°, 44°, 57°, and 64° corresponding to the respective hkl values (2 0 0), (3 1 1), (4 0 0), (5 1 1), and (4 4 0). The diffraction peaks of FeS matched with JCPDS # 75-2165, corresponding to the positions 29.9°, 34.7°, 43.2°, and 53.1°, having hkl values (1 1 0), (1 1 2), (1 0 5), and (3 0 0). The FeS–Fe_3O_4 composite shows all the distinct peaks of FeS, and Fe_3O_4, confirming the successful preparation of the composite material (Fig. 1a). Fig. 2b shows the BET surface area analysis and pore size distribution of the FeS–Fe_3O_4 nanocomposite. The adsorption–desorption isotherms show type IV behavior, which is typical of mesoporous materials. As the relative pressure approaches 1, the volume absorbed increases a lot. The BET surface area of the composite is predicted to be 34.21 m^2 g^{-1}, indicating a moderate surface area suitable for energy storage applications. The inset in Fig. 2b shows the pore size distribution, which is highest around 3–5 nm. This shows that the composite material has mesopores. These mesopores are useful for boosting the electrochemical performance of the FeS–Fe_3O_4 nanocomposite, as they provide additional surface area for charge storage. Nitrogen adsorption–desorption measurements reveal that both Fe_3O_4 and FeS exhibit typical type-IV isotherms with pronounced hysteresis loops, indicating their mesoporous nature. The BET surface areas of Fe_3O_4 (24.3 m^2 g^{-1}) and FeS (28.54 m^2 g^{-1}) confirm moderately porous

structures that facilitate electrolyte penetration and ion transport; further details are provided in the SI (Fig. S3a and b).

Fig. 3(a and a$_1$) shows the morphology of FeS, which exhibits distributed nanoparticles with rough surfaces; the particles show agglomeration with sharp edges, and the agglomerates show strong inter-particle interactions with limited porosity within the FeS structure. Fig. 3(b and b$_1$) display the SEM images of Fe_3O_4, revealing a relatively uniform morphology composed of near-spherical nanoparticles. These particles are closely packed and interconnected, forming chain-like and clustered assemblies. Compared to FeS, Fe_3O_4 exhibits a more homogeneous particle size distribution and smoother surfaces, indicating controlled nucleation and growth during synthesis. The interconnected nanoparticle network is beneficial for facilitating electron transport and structural stability. Fig. 3(c and c$_1$) shows the morphology of the FeS–Fe_3O_4 composite, where a distinct hybrid structure can be clearly observed. The composite displays a hierarchical and porous architecture formed by the intimate integration of FeS and Fe_3O_4 particles. The Fe_3O_4 nanoparticles are uniformly anchored onto the FeS matrix, resulting in a rough and highly textured surface with abundant interparticle voids. This interconnected and porous morphology provides an increased surface area and more accessible active sites, which can effectively enhance electrolyte penetration and ion diffusion. The strong interfacial contact between FeS and Fe_3O_4 is expected to improve charge transfer kinetics and structural integrity during electrochemical cycling. So, the FESEM analysis confirms the successful formation of the FeS–Fe_3O_4 composite with a well-integrated hierarchical morphology, which is advantageous for electrochemical energy storage applications due to its enhanced surface area, improved conductivity pathways, and robust structural framework.

Fig. 4a depicts the elemental representation of the FeS–Fe_3O_4 composite, with unique colors denoting all pertinent components, signifying the successful synthesis of the composite. The results are shown in dark red (Fe), purple (S), and blood red (O), showing the uniform distribution of the FeS–Fe_3O_4 composite. The last figure shows the EDX analysis of the FeS–Fe_3O_4

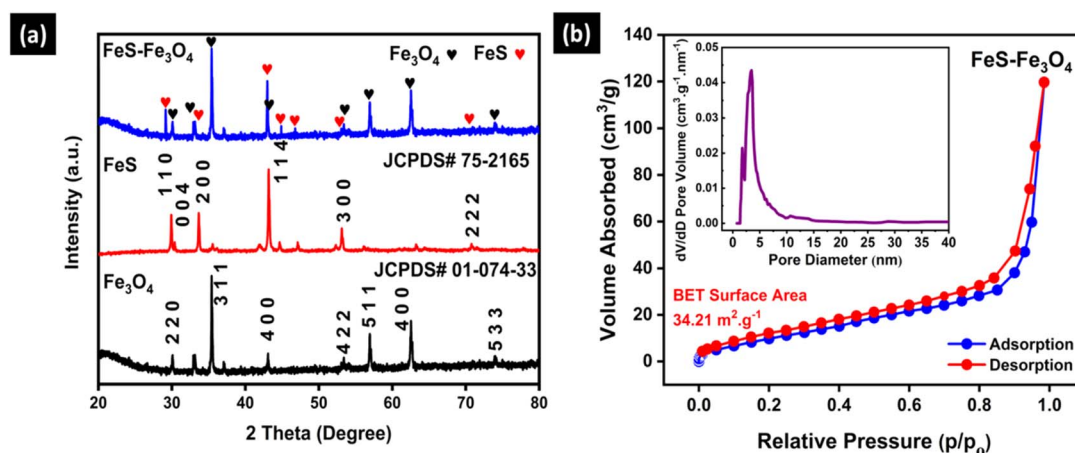Fig. 2 (a) X-ray diffraction of Fe_3O_4, FeS, and FeS–Fe_3O_4 composite. (b) BET analysis of the FeS–Fe_3O_4 composite.
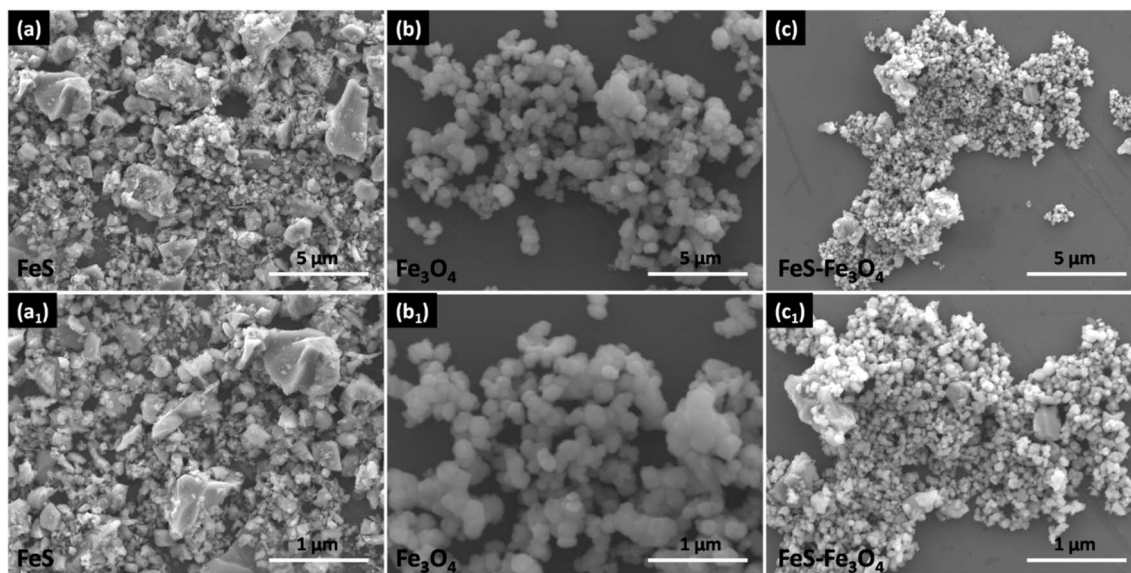
Fig. 3 Field emission scanning electron microscopy of FeS (a and a_1), Fe_3O_4 (b and b_1), and FeS–Fe_3O_4 composite (c and c_1).
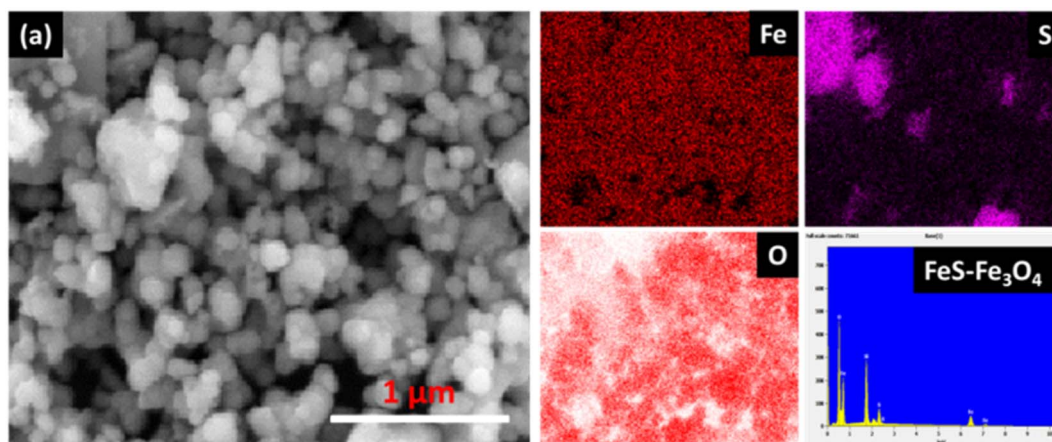

Fig. 4 (a) EDS mapping of the FeS–Fe_3O_4 composite with EDX attachment.

composite, confirming the successful formation of the FeS–Fe_3O_4 composite without any other additional peaks.

4. Electrochemical performance of FeS, Fe_3O_4, and FeS–Fe_3O_4 composite in a 3E system

Fig. 5a depicts a comparative cyclic voltammetry (CV) analysis of FeS, Fe_3O_4, and the FeS–Fe_3O_4 nanocomposite obtained at a scan rate of 20 mV s^{-1}. Fig. 5(b–d) further demonstrate the CV curves of Fe_3O_4, FeS, and the FeS–Fe_3O_4 nanocomposite, respectively, obtained at various scan rates ranging from 10 to 50 mV s^{-1} within a potential window of 0.0–0.8 V. The FeS–Fe_3O_4 nanocomposite has a CV profile that is almost rectangular even at a high scan rate 50 mV s^{-1}. This shows that it has excellent capacitive performance and fast charge transfer

kinetics. In contrast, the CV curves of pure FeS and Fe_3O_4 electrodes exhibit strong redox peaks and obvious distortions, indicating sluggish reaction kinetics and poor electrochemical reversibility during the redox process. The composite electrode FeS–Fe_3O_4 shows a large area under the curve, which means its conductivity is better than that of both pure Fe_3O_4 and FeS electrodes. The reason for the large area under the curve is that FeS is more conductive than Fe_3O_4, which provides more electrons during the CV test Fig. 5a. The results demonstrate that both pure FeS and Fe_3O_4 electrodes have different redox peaks centered around 0.4 V, which are associated with the reversible Fe^{2+}/Fe^{3+} redox processes.[47] The fact that these acute redox patterns are less pronounced in the composite further supports its better capacitive properties and faster electrochemical responsiveness. The following reactions are involved in the 3 M KOH solution during the CV test.
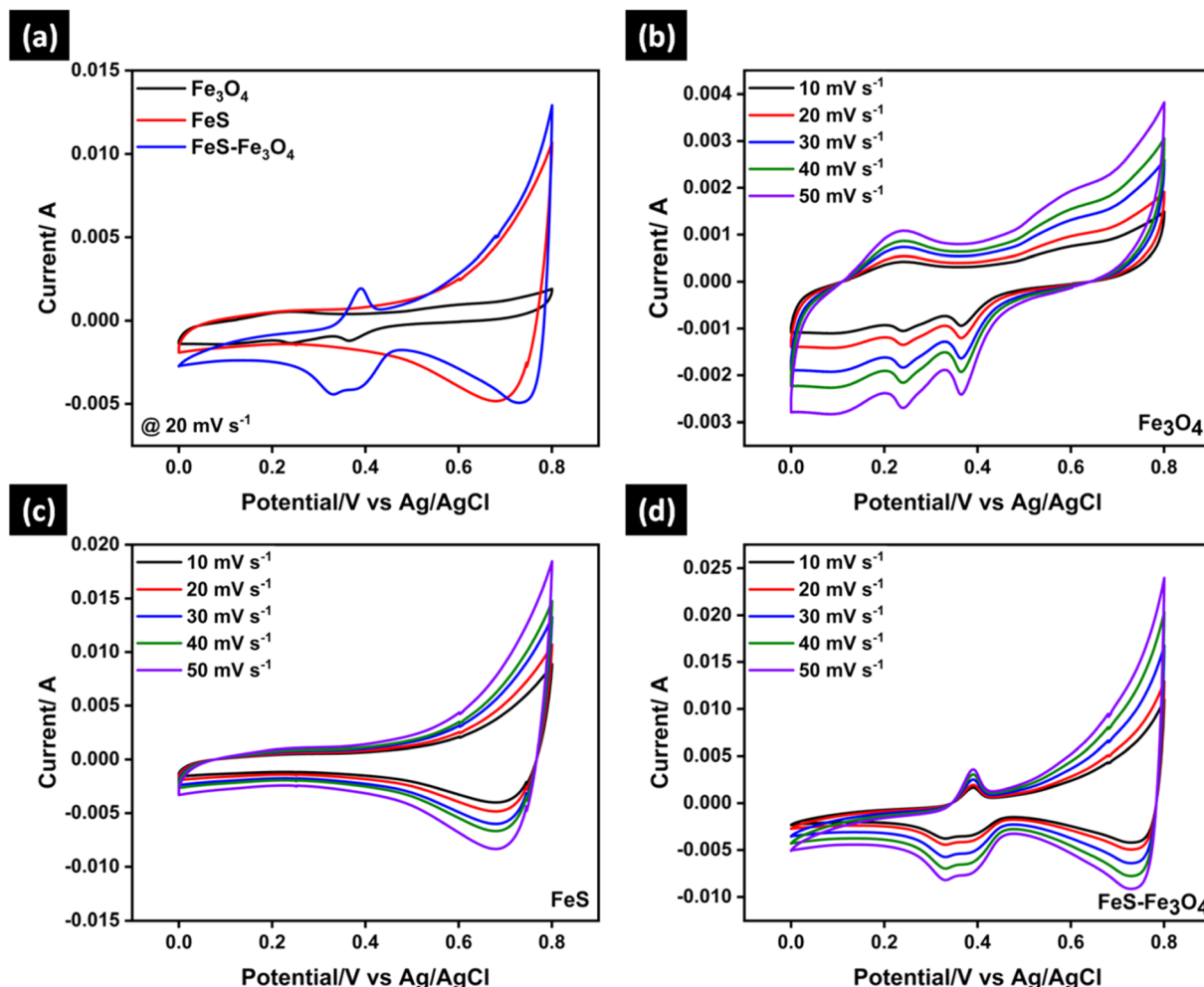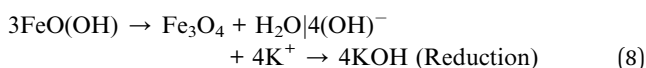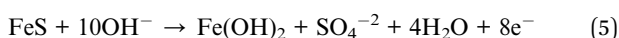
Fig. 5 (a) Comparative CV analysis of Fe_3O_4, FeS, and FeS–Fe_3O_4 composite at 20 mV s^{-1}, and CV analysis of (b) Fe_3O_4, (c) FeS, and (d) FeS–Fe_3O_4 nanocomposite at scan rates of 10 to 50 mV s^{-1}.

$$FeS + 10OH^- \rightarrow Fe(OH)_2 + SO_4^{-2} + 4H_2O + 8e^- \quad (5)$$

$$FeS + 8OH^- \rightarrow Fe(OH)_2 + SO_3^{-2} + 3H_2O + 6e^- \quad (6)$$

$$Fe_3O_4 + H_2O + (OH)^- \rightarrow 3FeO(OH)|4K^+ \text{ (Oxidation)} \quad (7)$$

$$3FeO(OH) \rightarrow Fe_3O_4 + H_2O|4(OH)^- + 4K^+ \rightarrow 4KOH \text{ (Reduction)} \quad (8)$$

In an alkaline electrolyte, reversible redox reactions involving both the FeS and Fe_3O_4 phases dictate the electrochemical characteristics of the FeS–Fe_3O_4 composite electrode. Eqn (7) and (8) show that the oxidation and reduction processes take place during the cyclic voltammetry analysis. In this reaction, FeS reacts with OH$^-$ hydroxide ions to make iron hydroxide Fe(OH)$_2$. At the same time, sulfur is transformed into SO_4^{2-} and electrons are released. When FeS reacts in KOH, it forms Fe(OH)$_2$ and oxidized sulfur, due to which at the electrode, the faradaic redox reaction occurs and the electrode acts like a pseudocapacitor, increasing the overall capacitance of the electrode.

The Fe_3O_4 phase also plays a big role in charge storage by using iron oxy-hydroxide species in reversible oxidation–reduction processes. Fe_3O_4 oxidizes in the presence of water and hydroxide ions, as shown in eqn (7), forming FeO(OH) and releasing electrons. This process involves the oxidation of Fe^{2+} to Fe^{3+}, which is a very important part of the faradaic charge-storage mechanism. During the cathodic scan, the reverse reaction happens, as given in eqn (8), where FeO(OH) is reduced back to Fe_3O_4 with the consumption of electrons and hydroxide ions, regenerating KOH in the electrolyte. This reversible transition between Fe_3O_4 and FeO(OH) ensures good redox reversibility and cycling stability.

The capacitive and diffusion-controlled charge storage contributions of the Fe_3O_4, FeS, and FeS–Fe_3O_4 composite electrodes were quantitatively examined at varied scan rates ranging from 10–50 mV s^{-1}, as reported in Table S1. For the Fe_3O_4 electrode, the charge storage behavior is largely dominated by diffusion-controlled mechanisms at all scan rates. At a low scan rate 10 mV s^{-1}, the diffusion contribution reaches 87%, while the capacitive contribution accounts for just 13%. With increasing scan rate, the capacitive contribution gradually

improves to 39% at 50 mV s^{-1}, indicating enhanced surface-controlled kinetics; nonetheless, diffusion-controlled behavior remains dominant, revealing the bulk redox nature of Fe$_3$O$_4$. In the case of the FeS electrode, a moderate increase in capacitive contribution is found compared to Fe$_3$O$_4$. At a scan rate of 10 mV s^{-1}, the capacitive contribution is 22%, increasing steadily to 48% at 50 mV s^{-1}, whereas the diffusion contribution declines from 78% to 52%. This pattern shows that FeS exhibits mixed charge storage behavior, where both surface redox reactions and diffusion-limited processes contribute significantly, perhaps because to its increased electrical conductivity relative to Fe$_3$O$_4$. Notably, the FeS–Fe$_3$O$_4$ nanocomposite electrode displays a much larger capacitive contribution across all scan rates. At 10 mV s^{-1}, the capacitive contribution already reaches 34%, which further increases to 66% at 50 mV s^{-1}, while the diffusion contribution similarly reduces from 66% to 34%. The relationship was utilized to precisely quantify the contributions of diffusion-controlled and capacitive processes.

$$i(V) = K_1 v + K_2 v^{1/2} \tag{9}$$

This equation indicates that the surface capacitive effects are represented by $K_1 v$, whereas the diffusion-controlled insertion process is denoted by $K_2 v_{1/2}$. Rearranging the sequence of the equation:

$$\frac{i(V)}{v^{1/2}} = K_1 v^{1/2} + K_2 \tag{10}$$

This dramatic shift toward capacitive-controlled behavior underlines the synergistic interaction between FeS and Fe$_3$O$_4$. The greater capacitive response can be due to enhanced electrical conductivity, increased electrochemically active surface area, and quicker ion transport at the hetero interface between the two phases. Overall, the FeS–Fe$_3$O$_4$ composite demonstrates a dominant surface-controlled charge storage mechanism at higher scan rates, which is particularly desirable for high-rate energy storage applications. The enhanced capacitive contribution verifies faster reaction kinetics and improved reversibility, explaining the superior electrochemical performance of the composite compared to the individual FeS and Fe$_3$O$_4$ electrodes (Fig. 6).

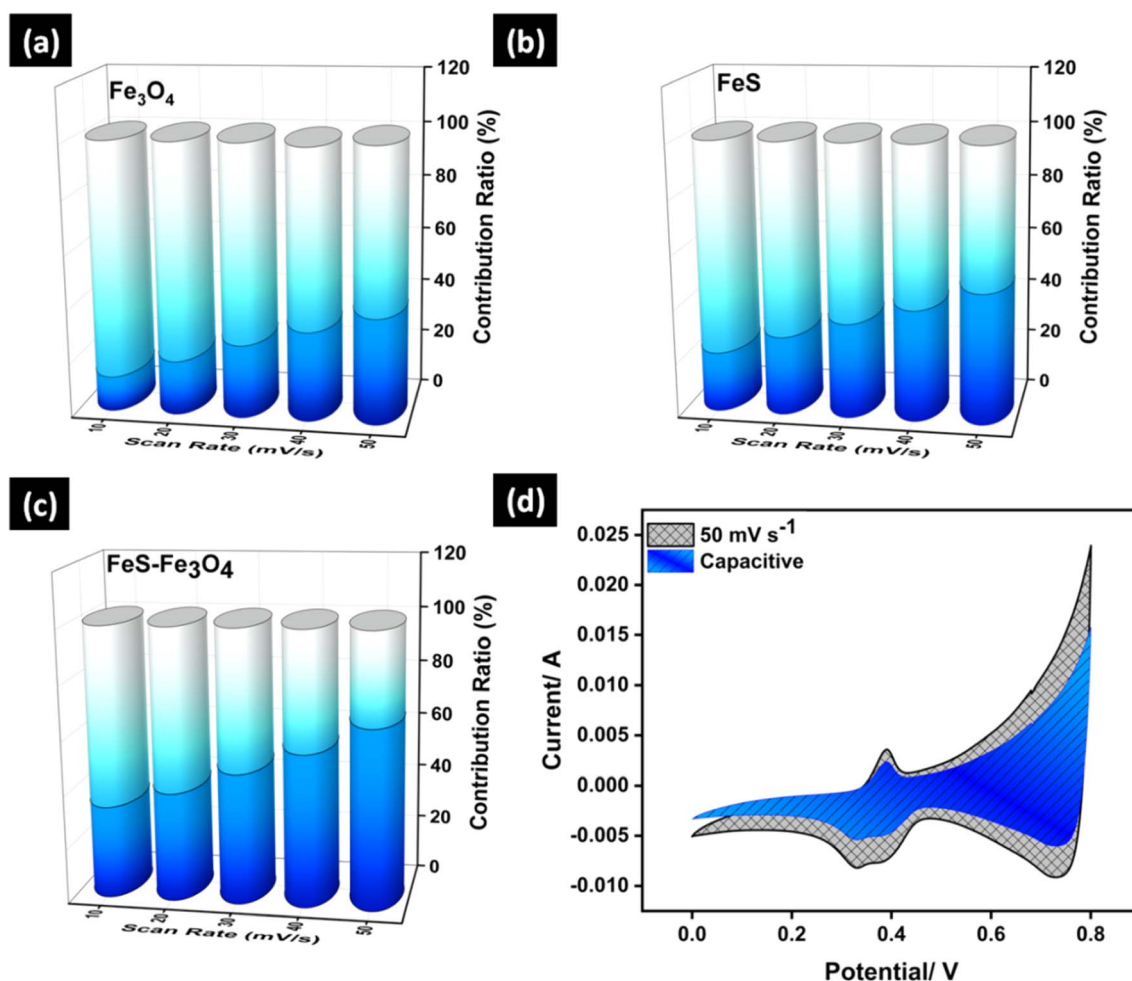Fig. 6 Capacitive–diffusion analysis of (a) Fe$_3$O$_4$, (b) FeS, and (c) FeS–Fe$_3$O$_4$ composite at 10–50 mV s^{-1} and (d) CV analysis of FeS–Fe$_3$O$_4$ at 50 mV s^{-1} with marked capacitive and diffusion contributions.

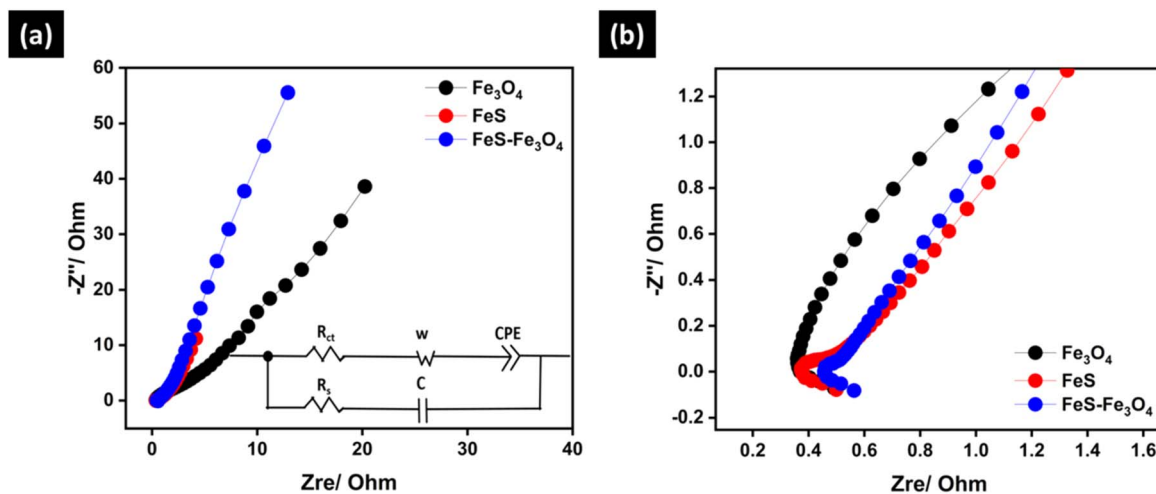**Fig. 7** EIS analysis of (a) Fe_3O_4, FeS, and FeS–Fe_3O_4 composite, and the (b) zoomed-in view.

Fig. 7 shows the electrochemical impedance parameters found for the Fe_3O_4, FeS, and FeS–Fe_3O_4 composite electrodes. The three electrodes have nearly equal solution resistance (R_s) values. This means that the electrolyte resistance is about the same and that the electrode materials and the current collector have good electrical contact. The R_s value for the Fe_3O_4 electrode is 0.49 Ω, while the R_s values for FeS and the FeS–Fe_3O_4 composite are 0.50 Ω and 0.56 Ω, respectively. There is a considerable difference in the charge transfer resistance (R_{ct}) between the electrodes. The R_{ct} value of the Fe_3O_4 electrode is 2.34 Ω, which means that charge transfer at the point where the electrode and electrolyte come in contact is slow. The FeS electrode has a much lower R_{ct} of 0.54 Ω, indicating higher conductivity and faster electron transport between surfaces. The R_{ct} value of the FeS–Fe_3O_4 composite electrode is 0.55 Ω, which is much lower than that of pure Fe_3O_4 and similar to that of FeS. FeS serves as an efficient electronic pathway, ensuring rapid electron transport across the electrode, while also providing structural support that mitigates mechanical stress and suppresses agglomeration of Fe_3O_4 during cycling. Most importantly, the FeS–Fe_3O_4 composite induces interfacial polarization and electronic redistribution, creating abundant electrochemically active sites and accelerating interfacial redox reactions.[52] The impedance results reveal that the creation of the FeS–Fe_3O_4 composite significantly boosts interfacial charge transfer while preserving low solution resistance, which leads to the higher electrochemical performance, observed for the composite electrode (Table 1).

Fig. 8 shows the charge–discharge behavior of Fe_3O_4, FeS, and the FeS–Fe_3O_4 composite electrodes in a 3 M KOH electrolyte. At a current density of 2 A g^{-1} and in a potential window of (0.0–0.8) V, Fig. 8a compares the GCD curves of the three electrodes. The FeS–Fe_3O_4 composite has a substantially longer discharge time than the other electrodes, which means that it can store more charge than pure Fe_3O_4 and FeS. This enhanced performance is due to the synergistic interaction between FeS and Fe_3O_4, which facilitates charge transfer and ion diffusion. Fig. 8(b–d) show the GCD curves for Fe_3O_4, FeS, and the FeS–Fe_3O_4 composite at current densities of 1, 2, 3, and 4 A g^{-1}. The charge and discharge curves of the Fe_3O_4 electrode (Fig. 8b) are comparable to each other. But when the current density gets higher, the discharge time gets shorter, which indicates that the rate capability is limited. The FeS electrode in Fig. 8c shows a similar pattern. When the current density is higher, the discharge time is shorter, leading to higher polarization. This illustrates that electrochemical kinetics are limited. The GCD curves for the FeS–Fe_3O_4 composite electrode (Fig. 8d) are clear and highly symmetrical, even at high current densities. This means that it can be readily reversed and operates better at higher rates. The lower voltage drop and longer discharge time indicate that the composite structure has better electrical conductivity and faster ion transport. Fig. 8e summarizes the specific capacitance values of all electrodes calculated from the GCD curves at different current densities; for details, see Table 2. At 1 A g^{-1}, the FeS–Fe_3O_4 composite delivers a high specific capacitance of 464.6 F g^{-1}, which is substantially higher than that of Fe_3O_4 (88.13 F g^{-1}) and FeS (94.5 F g^{-1}). Even at higher current densities of 2, 3, and 4 A g^{-1}, the composite retains capacitance values of 449.5, 307.1, and 186.9 F g^{-1}, respectively, demonstrating superior rate capability. In comparison, both Fe_3O_4 and FeS electrodes suffer from a more pronounced decline in capacitance with increasing current density. The outstanding electrochemical performance of the FeS–Fe_3O_4 composite can be attributed to the combined effects of enhanced conductivity from FeS and the high pseudocapacitive

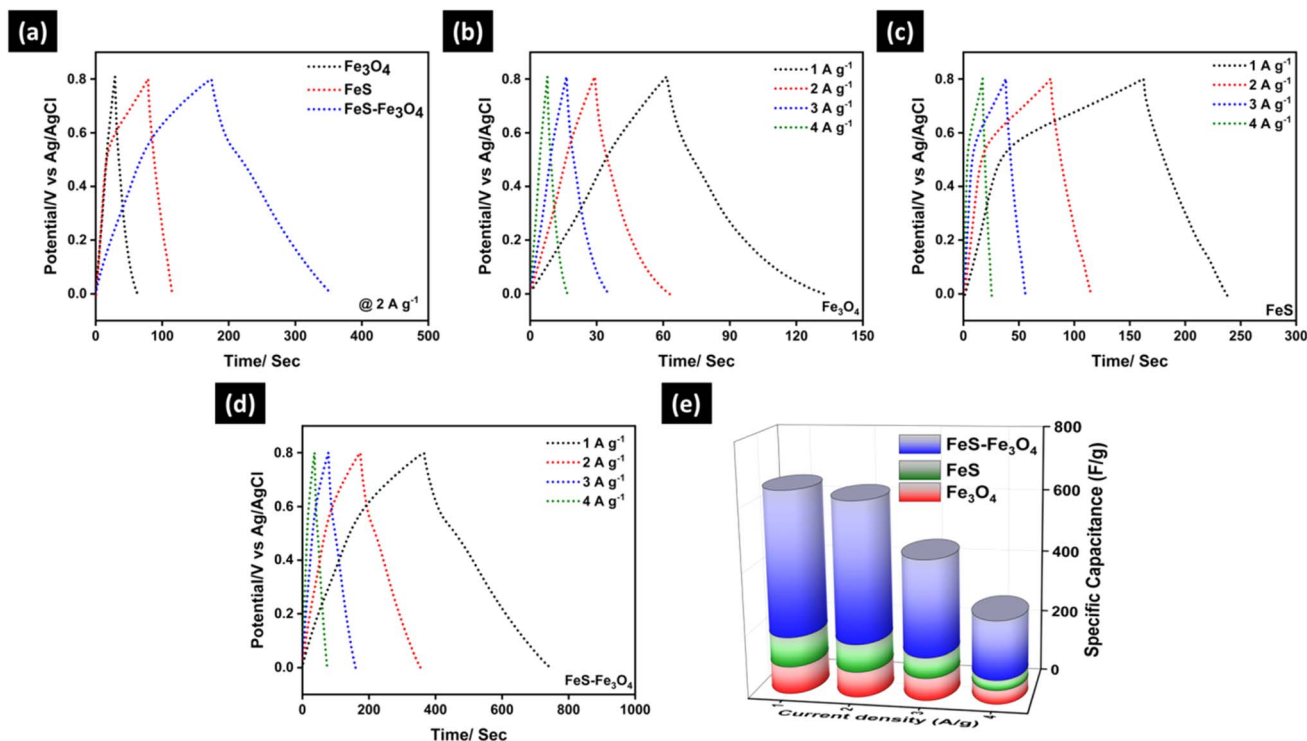**Table 1** The R_s, and R_{ct} values of Fe_3O_4, FeS, and FeS–Fe_3O_4 nanocomposite electrodes

Electrodes	R_s (Ω)	R_{ct} (Ω)
Fe_3O_4	0.49	2.34
FeS	0.50	0.54
FeS–Fe_3O_4 composite	0.56	0.55

Fig. 8 (a) Comparative GCD analysis of Fe_3O_4, FeS, and FeS–Fe_3O_4 composite at 2 A g^{-1}, and GCD of (b) Fe_3O_4, (c) FeS, and (d) FeS–Fe_3O_4 composite at 1–5 A g^{-1}, and (e) specific capacitance of all prepared electrodes at 1–5 A g^{-1}.

Table 2 Specific capacitance of Fe_3O_4, FeS, and FeS–Fe_3O_4 nanocomposite electrodes in 3 M KOH solutions

Current density A g^{-1}	Fe_3O_4 F g^{-1}	FeS F g^{-1}	FeS–Fe_3O_4 F g^{-1}
1	88.13	94.5	464.6
2	81.43	88.3	449.5
3	72.10	65.5	307.1
4	44.65	32.1	186.9

contribution of Fe_3O_4, along with improved electrolyte accessibility and structural stability.

5. Electrochemical performance of the asymmetric FeS–Fe_3O_4//AC supercapacitor

Fig. 9 presents the electrochemical performance of the assembled asymmetric supercapacitor device based on the FeS–Fe_3O_4 composite as the positive electrode and activated carbon (AC) as the negative electrode, evaluated in a 3 M KOH electrolyte. Fig. 9a shows the CV window of both AC (−0.6 to 0.0) V and FeS–Fe_3O_4 composite (0.0 to 0.8) V at a scan rate of 20 mV s^{-1} in 3 M KOH solution. The CV shape of AC is rectangular, showing its EDLC behaviour, while the FeS–Fe_3O_4 composite shows pseudocapacitive behaviour with a broader response due to reversible redox reactions. The suitable window for both AC and FeS–Fe_3O_4 composite confirms the construction of the

asymmetric device for practical applications. Fig. 9b shows the CV analysis of the FeS–Fe_3O_4//AC device at various scan rates ranging from 10–100 mV s^{-1} in a potential window of 0.0 to 1.4 V. As the scan rate increases from 10–100 mV s^{-1}, the area under the curve also increases, which shows that the electrochemical performance can be reversed easily and the transportation of charge happens quickly. The shape of the CV remains the same at high scan rates, which shows the good stability of the FeS–Fe_3O_4//AC device in 3 M KOH solution. Fig. 9c shows the galvanostatic charge–discharge curve at a current density of 1–5 A g^{-1}. The CD curve remains the same even at a very small voltage drop. This shows that the device has high coulombic efficiency and excellent reversibility over repeated cycles. Fig. 9d shows the particular capacitance values that were found from the GCD curves at various current densities. At 1 A g^{-1}, the device has a high specific capacitance of 169.29 F g^{-1}, which slowly drops to 110.85 F g^{-1} at 5 A g^{-1} (for details see Table 3). This shows that it can operate effectively at high current densities. As the current density goes up, the energy density goes down from 46.10 to 30.17 Wh kg^{-1}, while the power density goes up from 699.6 to 3998.4 W kg^{-1}. This shows that the energy–power performance is very well balanced. Fig. 9e shows the coulombic efficiency of the FeS–Fe_3O_4//AC device at different current densities. The device has a high coulombic efficiency of about 102% at low current densities and it remains above 95% even at higher current densities. This means that it can charge and discharge quickly and doesn't lose much energy while it works. Fig. 9f shows the EIS analysis performed for the FeS–Fe_3O_4//AC device. The Nyquist plot

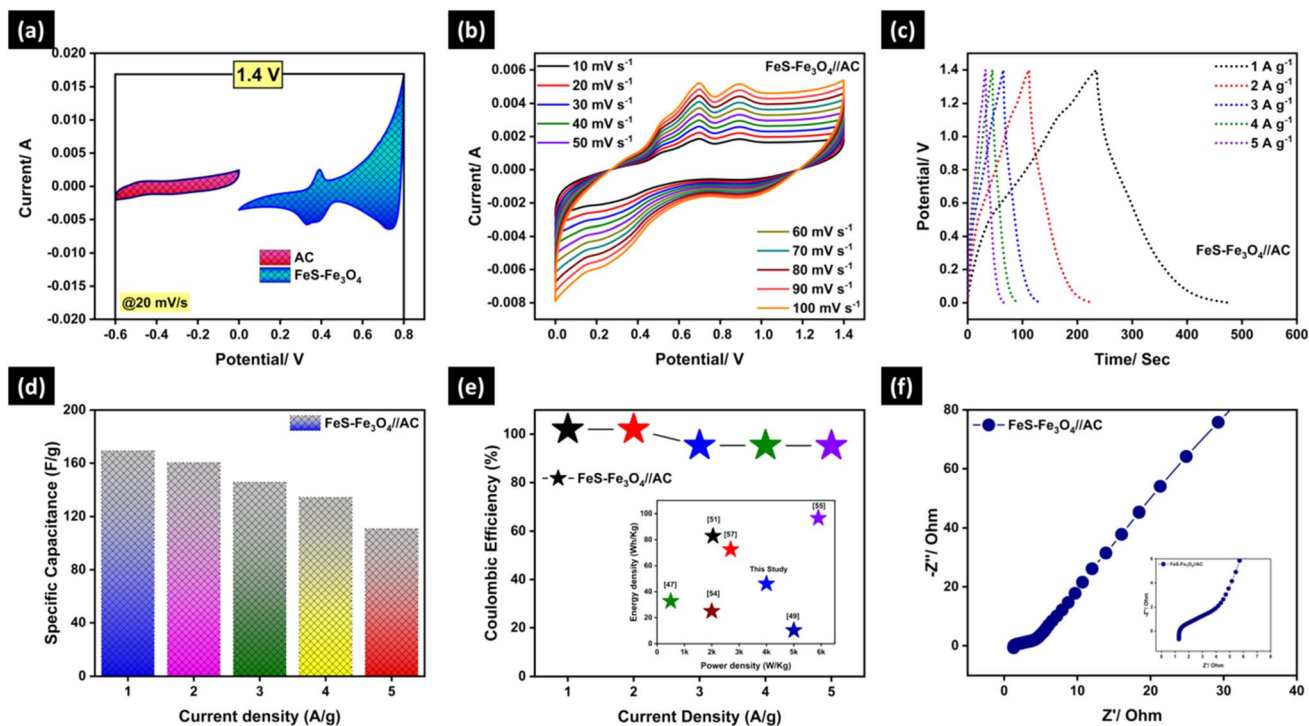**Fig. 9** Asymmetric device analysis of FeS–Fe$_3$O$_4$//AC: (a) CV window of the FeS–Fe$_3$O$_4$ composite device, (b) CV analysis at 10–100 mV s^{-1}, (c) GCD analysis at 1–5 A g^{-1}, (d) specific capacitance of the tdevice, (e) coulombic efficiency ofhe device at 1–5 A g^{-1}, and (f) EIS analysis.

Table 3 Specific capacitance, energy density, power density, and coulombic efficiency of the asymmetric FeS–Fe$_3$O$_4$//AC device at a current density of 1–5 A g^{-1}

Current density (A g^{-1})	Specific capacitance (F g^{-1})	Energy density (Wh kg^{-1})	Power density (W kg^{-1})	Coulombic efficiency (%)
1	169.29	46.10	699.6	102
2	160.50	43.62	1401.1	102
3	145.71	39.59	2098.4	95.3
4	134.28	36.45	2801.2	95.3
5	110.85	30.17	3998.4	95.2

shows that R_s is 1.27 ohms, which shows that the 3 M KOH electrolyte has strong ionic conductivity with low internal resistance. The low charge transfer resistance (R_{ct}) of 3.96 ohm shows fast electron transport inside the device. So, from all the above results, it is clear that the FeS–Fe$_3$O$_4$//AC device is a promising device for energy storage applications.

Fig. 10 shows the cycling stability, energy density *vs.* power density, and coulombic efficiency of the prepared asymmetric device (FeS–Fe$_3$O$_4$//AC). Fig. 10a shows the cycling stability of the asymmetric device over 12 000 continuous charge–discharge cycles at a current density of 7 A g^{-1}. The device retains 98.6% of its initial capacitance after prolonged cycling, demonstrating its excellent electrochemical durability and structural stability. The high retention confirms that the FeS–Fe$_3$O$_4$ nanocomposite and AC maintain strong interfacial integrity during the repeated redox reactions. Fig. 10b shows the energy density and power density of the asymmetric device at a current density of 1–5 A g^{-1}. The device attains a highest energy density of 46.10 Wh

kg^{-1}, with a power density of 699.6 W kg^{-1}. At high current density, the energy density reaches a value of 30.17 Wh kg^{-1}, and power density reaches 3998.4 W kg^{-1}, highlighting its excellent rate capability. This favorable balance between energy and power densities reflects the synergistic contribution of the pseudocapacitive FeS–Fe$_3$O$_4$ composite and the electric double-layer behavior of the AC electrode, making the device suitable for high-power energy storage applications. Fig. 10c shows how well the FeS–Fe$_3$O$_4$//AC device works after 12 000 charge–discharge cycles. During the entire cycling test, the coulombic efficiency remains rather steady at about 99.8%. This indicates that electrochemical reactions are highly reversible and involve very little energy (more details can be seen in Table S2). The asymmetric device's extraordinary efficiency further confirms its superb charge transfer kinetics and long-term stability. These findings demonstrate the FeS–Fe$_3$O$_4$//AC asymmetric supercapacitors' energy–power characteristics, high efficiency, and great cycle stability. This shows that it has a lot of potential
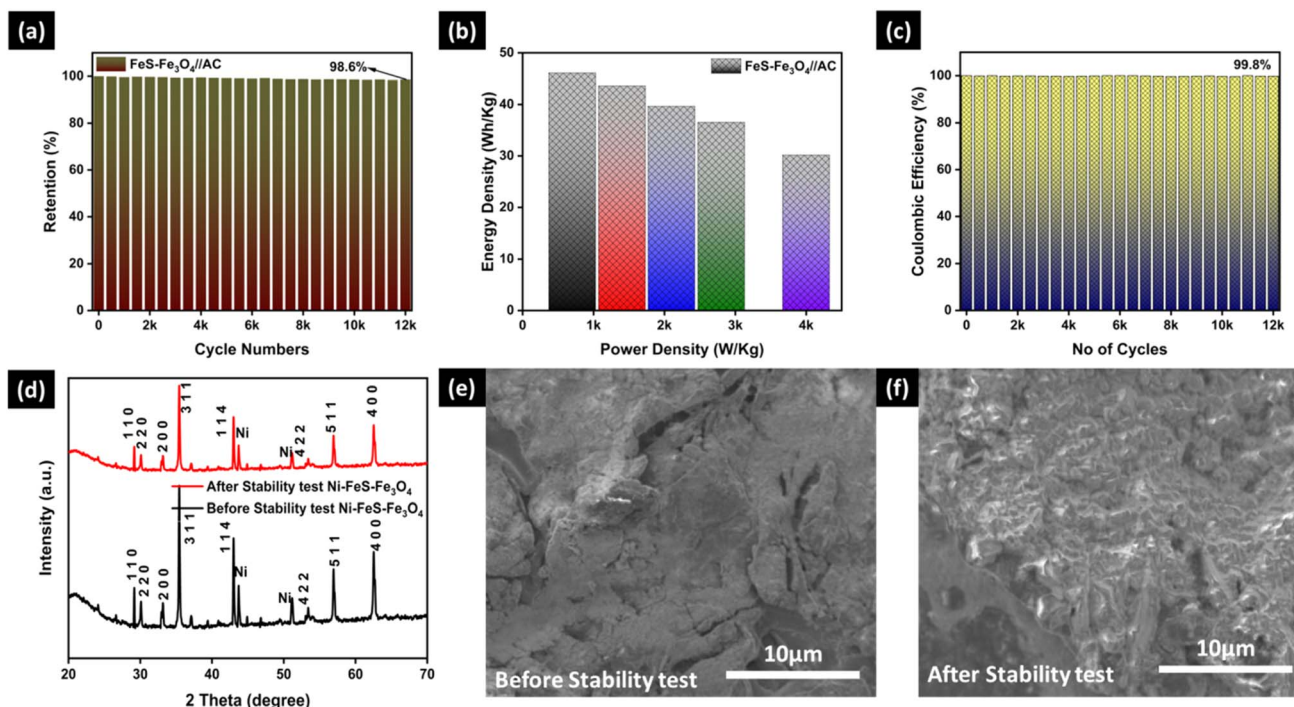
Fig. 10 (a) Cycling stability of the Fes−Fe$_3$O$_4$//AC asymmetric device over 12k cycles at 7 A g^{-1}, (b) energy density vs. power density, (c) coulombic efficiency over 12k cycles, (d) XRD analysis of FeS−Fe$_3$O$_4$ before and after the stability test, (e) SEM before the stability test, and (f) SEM after the stability test.

for use in the future as a way to store energy in a way that doesn't harm the environment. Fig. 10d displays the XRD analysis of the FeS–Fe$_3$O$_4$ composite before and after the stability test. The peaks of the FeS–Fe$_3$O$_4$ composite matched with the characteristic planes of FeS and Fe$_3$O$_4$, which confirms the successful formation of the composite. Two peaks are also observed, which belong to Ni-foam. After the stability test, the intensity reduced slightly, but all the peaks confirm the good crystallinity of the FeS–Fe$_3$O$_4$ composite. Fig. 10(e and f) shows the SEM image of the FeS–Fe$_3$O$_4$ composite on Ni-foam before and after the stability test at 10 μm. The electrode before the stability test shows a comparatively smooth surface, and after the stability test, it shows a well distributed active material that provides sufficient active sites for efficient ion transfer in 3 M KOH electrolyte. The FESEM image after the stability test shows that the overall morphology of the FeS–Fe$_3$O$_4$ composite is well preserved. Although minor surface roughening and agglomeration of particles are observed, no structural collapse occurs. The maintained morphology after 12 K cycles further confirms the mechanical robustness and electrochemical performance of the FeS–Fe$_3$O$_4$ composite electrode.

6. Conclusion

In summary, a FeS–Fe$_3$O$_4$ nanocomposite was successfully synthesized and systematically investigated as an efficient electrode material for advanced supercapacitor applications. Structural and morphological characterization confirmed the formation of a well-integrated heterostructure composed of crystalline FeS and Fe$_3$O$_4$ phases, providing abundant electroactive sites and a favourable architecture for rapid ion transport. Electrochemical evaluations demonstrated that the FeS–Fe$_3$O$_4$ composite delivers significantly enhanced capacitive performance compared to the individual FeS and Fe$_3$O$_4$ electrodes, achieving a high specific capacitance of 464.6 F g^{-1} at 1 A g^{-1} and maintaining good rate capability at higher current densities. The improved electrochemical behaviour is primarily attributed to the synergistic interaction between the high electrical conductivity of FeS and the strong pseudocapacitive contribution of Fe$_3$O$_4$, which together facilitate fast charge transfer and efficient redox reactions. Furthermore, an asymmetric supercapacitor device assembled using the FeS–Fe$_3$O$_4$ nanocomposite as the positive electrode and activated carbon as the negative electrode operated stably over an extended voltage window of 1.4 V in 3 M KOH electrolyte. The device exhibited a high energy density of 46.10 Wh kg^{-1} at a power density of 699.6 W kg^{-1} and retained 30.17 Wh kg^{-1} at a high power density of 3998.4 W kg^{-1}. Remarkably, the device maintained 98.6% capacitance retention and a coulombic efficiency of approximately 99.8% after 12 000 charge–discharge cycles, highlighting its excellent long-term stability and reversibility. Overall, this study demonstrates that the FeS–Fe$_3$O$_4$ nanocomposite is a promising electrode material for high-performance, durable, and practical energy storage systems.

Author contributions

Junaid Riaz: wrote the original manuscript draft, data creation, characterization, and electrochemical analysis. Muhammad Arif: supervision, review and editing, formal analysis. Ghulam

Murtaza: software analysis. Zahra Bayhan: review and editing, Amina Bibi: supervision, review and editing, characterization, and formal analysis.

Conflicts of interest

The authors declare that they have no conflict of interest.

Data availability

The data that have been used are confidential & will be available on request.

Supplementary information (SI) is available. See DOI: https://doi.org/10.1039/d5na01165e.

Acknowledgements

References

1 S. Banerjee, B. Mordina, P. Sinha and K. K. Kar, Recent advancement of supercapacitors: A current era of supercapacitor devices through the development of electrical double layer, pseudo and their hybrid supercapacitor electrodes, *J. Energy Storage*, 2025, **108**, 115075.

2 M. Arif, J. Riaz, A. Bibi, H. Yang and T. Zhu, Enhancing supercapacitor energy density by TiN–ZnS composites unveiled as a promising electrode, *APL Mater.*, 2024, **12**(7), DOI: 10.1063/5.0221353.

3 F. Hu, J. Wei, X. Quan and Q. Ouyang, Rational design of defect-rich MoS2-modified V2CTx electrodes for advanced flexible supercapacitor, *Chem. Eng. J.*, 2025, 170003.

4 M. Arif, J. Riaz, H. Yang, Z. Fu, A. Bibi and T. Zhu, Synthesis of high-performance CdS/MnO composite electrode to achieve high energy and power densities for asymmetrical supercapacitors, *Mater. Des.*, 2025, **251**, 113704.

5 J. Riaz, W. Yongyuan, J. Cao, A. Bibi, D. Muhammad, H. Eman and X. Zhou, Wet-chemical synthesized TiN-CuO nanocomposite: Advancing supercapacitor technology with high energy and power density, *Phys. E*, 2025, **165**, 116105.

6 A. F. Kassem, N. U. Hassan, M. Jelani, E. A. M. Saleh, M. M. Moharam, R. H. Althomali, *et al.*, Superior supercapattery performance enabled by MnS/Fe2O3 nanosheets and theoretical evaluation of contributing currents, *Inorg. Chem. Commun.*, 2025, **176**, 114171.

7 J. Riaz, Y. Zhang, J. Cao, A. Bibi, M. Arif, Z. Zhang, *et al.*, Facile synthesis of TiN nano sheets decorated Fe2O3 nanoparticles as novel cathode material for Asymmetric Supercapacitor, *Surf. Interfaces*, 2024, **46**, 104080.

8 A. F. Kassem, N. U. Hassan, E. A. M. Saleh, R. Hasan, M. M. Moharam, R. H. Althomali, *et al.*, Al intercalated ZnS nanosheets as anode for supercapattery application with wide operating potential window, *Inorg. Chem. Commun.*, 2025, **171**, 113588.

9 J. Riaz, J. Cao, Y. Zhang, A. Bibi and X. Zhou, Facile synthesis and electrochemical analysis of TiN-based ZnO nanoparticles as promising cathode materials for asymmetric supercapacitors, *Nanoscale Adv.*, 2024, **6**(20), 5145–5157.

10 K. M. Albalawi, M. Al-Dossari, A. M. Saeedi, R. H. Althomali, G. F. Solre, M. Sadiq and S. U. Asif, Synergistic effects of scandium doping and N-rGO integration on titanium oxide and evaluating faradic/non-faradic behavior by Dunn's model for high-performance supercapattery applications, *J. Energy Storage*, 2024, **104**, 114576.

11 J. Riaz, J. Cao, A. Bibi, M. Arif and D. Muhammad, Hydrothermal synthesis of ball-like ZnS nanospheres decorated urchin-like W18O49 nanospheres as electrode for high power and stable hybrid supercapacitor, *Mater. Lett.*, 2024, **370**, 136853.

12 J. Riaz, Y. Zhang, J. Cao, A. Bibi, Z. Zhang and X. Zhou, High-performance electrode material synthesis via wet-chemical method: A study on NbN–Fe2O3 composite, *J. Mater. Sci.: Mater. Electron.*, 2024, **35**(17), 1176.

13 J. Riaz, J. Cao, Y. Zhang, A. Bibi, M. Arif, Z. Zhang, *et al.*, Improved performance of TiN nano buds decorated MoS2 sheets in asymmetric supercapacitors, *J. Mater. Sci.: Mater. Electron.*, 2024, **35**(17), 1142.

14 M. M. Moharam, S. U. Asif, E. A. M. Saleh, R. H. Althomali, A. F. Kassem and M. Sadiq, Tailoring electrochemical properties of zirconium oxide doped by praseodymium coated with carbon-based materials for superior supercapacitors, *Inorg. Chem. Commun.*, 2024, **169**, 113114.

15 D. Muhammad, H. Hou, K. M. Alotaibi, N. Ali, M. M. Al-Hinaai, J. Riaz, *et al.*, Improved Asymmetric Supercapacitors Using a Novel Synthesis of Organized FeS/SnS2 Nanostructure Effective Cathode Material, *J. Electron. Mater.*, 2025, **54**(3), 1972–1984.

16 M. Sadiq, M. U. Islam, M. M. Moharam, E. A. M. Saleh and S. U. Asif, Enhanced electrochemical performance of La2S3/N-rGO/PANI nanocomposites as an efficient electrode material for supercapacitor applications, *J. Mater. Sci.: Mater. Electron.*, 2024, **35**(15), 1011.

17 D. Muhammad, X. Liu, H. Hou, X. Yu, J. Rong, J. Riaz, *et al.*, Novel synthesis of systematized FeS/CuO nanostructure efficacious electrode material for escalating asymmetric supercapacitors, *J. Alloys Compd.*, 2025, **1016**, 178877.

18 T. Anwar, T. Manzoor, N. Hussain, S. N. Shah, S. Perveen, S. U. Asif, *et al.*, Antimony trisulfide with graphene oxide coated titania nanotube arrays as anode material for lithium-ion batteries, *J. Inorg. Organomet. Polym. Mater.*, 2024, **34**(10), 4780–4787.

19 J. Riaz, J. Cao, N. Hakimi, A. Sikandar, F. Aslam, T. Huma and A. Bibi, Synthesis of high-performance supercapacitor electrode materials by wet-chemical route based on TiN–Al2O3 composite, *J. Mater. Sci.: Mater. Electron.*, 2025, **36**(35), 2257.

20 J. Riaz, F. Aslam, M. Arif, T. Huma and A. Bibi, First investigation of high-performance FeS-based W18O49

asymmetric supercapacitors operating at 1.6 V, *Nanoscale Adv.*, 2025, **7**(1), 231–241.

21 Y. Tan, H. Lin, Z. Chen, L. Niu and H. Li, Regulating the coordination microenvironment of atomic bismuth sites in nitrogen-rich carbon nanosheets as anode for superior potassium-ion batteries, *J. Energy Chem.*, 2024, **99**, 365–374.

22 R. Wang, S. Luo, C. Xiao, Z. Chen, H. Li, M. Asif, *et al.*, MXene-carbon nanotubes layer-by-layer assembly based on-chip micro-supercapacitor with improved capacitive performance, *Electrochim. Acta*, 2021, **386**, 138420.

23 W. Zhu and D. Shen, Synthesis of Bi2O3/hierarchical porous carbon composites for supercapacitor application, *J. Energy Storage*, 2024, **79**, 110118.

24 J. Zhao, L. Yang, R. Li and Y. Zhou, One-Step Synthesis of Fe-Based Metal–Organic Framework (MOF) Nanosheet Array as Efficient Cathode for Hybrid Supercapacitors, *Inorganics*, 2023, **11**(4), 169.

25 Z. Chen, H. Lin, Y. Tan, L. Niu and H. Li, Anchoring Multi-Coordinated Bismuth Metal Atom Sites on Honeycomb-Like Carbon Rods Achieving Advanced Potassium Storage, *Adv. Funct. Mater.*, 2024, **34**(45), 2407653.

26 G. Qin, Y. Zhang, Z. Qi and X. He, Dynamically Reversible Gelation of Electrolyte for Efficient Wide-Temperature Adaptable Energy Storage, *Adv. Funct. Mater.*, 2024, **34**(28), 2316813.

27 M. Sethi, H. Bantawal, U. S. Shenoy and D. K. Bhat, Eco-friendly synthesis of porous graphene and its utilization as high performance supercapacitor electrode material, *J. Alloys Compd.*, 2019, **799**, 256–266.

28 M. Sethi, U. S. Shenoy, S. Muthu and D. K. Bhat, Facile solvothermal synthesis of NiFe2O4 nanoparticles for high-performance supercapacitor applications, *Front. Mater. Sci.*, 2020, **14**(2), 120–132.

29 M. Sethi, U. S. Shenoy and D. K. Bhat, Porous graphene–NiCo2O4 nanorod hybrid composite as a high performance supercapacitor electrode material, *New J. Chem.*, 2020, **44**(10), 4033–4041.

30 J. Sun, C. Xu and H. Chen, A review on the synthesis of CuCo2O4-based electrode materials and their applications in supercapacitors, *J. Materiomics*, 2021, **7**(1), 98–126.

31 M. Iqbal, N. G. Saykar, A. Arya, I. Banerjee, P. S. Alegaonkar and S. K. Mahapatra, High-performance supercapacitor based on MoS2@ TiO2 composite for wide range temperature application, *J. Alloys Compd.*, 2021, **883**, 160705.

32 F. Ahmad, A. Shahzad, M. Danish, M. Fatima, M. Adnan, S. Atiq, *et al.*, Recent developments in transition metal oxide-based electrode composites for supercapacitor applications, *J. Energy Storage*, 2024, **81**, 110430.

33 E. Sohouli, H. Teymourinia, A. Ramazani and K. Adib, Preparation of high-performance supercapacitor electrode with nanocomposite of CuO/NCNO flower-like, *Sci. Rep.*, 2023, **13**(1), 16221.

34 M. Sethi, U. S. Shenoy and D. K. Bhat, Hassle-free solvothermal synthesis of NiO nanoflakes for supercapacitor application, *Phys. B*, 2021, **611**, 412959.

35 T. P. Ramesh, U. S. Shenoy and D. K. Bhat, Exploring the potential of CoAl2O4 nanoflakes in supercapacitor applications, *J. Alloys Compd. Commun.*, 2025, 100111.

36 A. Kumar, H. K. Rathore, D. Sarkar and A. Shukla, Nanoarchitectured transition metal oxides and their composites for supercapacitors, *Electrochem. Sci. Adv.*, 2022, **2**(6), e2100187.

37 M. A. Rehman, S. Park, M. F. Khan, M. F. Bhopal, G. Nazir, M. Kim, *et al.*, Development of directly grown-graphene–silicon Schottky barrier solar cell using co-doping technique, *Int. J. Energy Res.*, 2022, **46**(8), 11510–11522.

38 M. Sethi, U. S. Shenoy and D. K. Bhat, Iron Oxide-Functionalized Graphene Nanocomposites for Supercapacitor Application, in *Iron Oxide-Based Nanocomposites and Nanoenzymes: Fundamentals and Applications*, Springer International Publishing, Cham, 2024, p. 77–117.

39 J. Xu, D. Wang, Y. Yuan, W. Wei, L. Duan, L. Wang, *et al.*, Polypyrrole/reduced graphene oxide coated fabric electrodes for supercapacitor application, *Org. Electron.*, 2015, **24**, 153–159.

40 T. Yamashita and P. Hayes, Analysis of XPS spectra of Fe2+ and Fe3+ ions in oxide materials, *Appl. Surf. Sci.*, 2008, **254**(8), 2441–2449.

41 X. Rui, H. Tan and Q. Yan, Nanostructured metal sulfides for energy storage, *Nanoscale*, 2014, **6**(17), 9889–9924.

42 C. Wang, S. Hu, J. Wang, S. Yao, C. Wang and Y. Wang, Fe3O4 loaded on the porous N-doped carbon spheres used as a high-performance anode material for lithium-ion batteries, *Ionics*, 2025, 1–14.

43 F. Reyes-Ortega, A. V. Delgado and G. R. Iglesias, Modulation of the magnetic hyperthermia response using different superparamagnetic iron oxide nanoparticle morphologies, *Nanomaterials*, 2021, **11**(3), 627.

44 S. Pal, S. Majumder, S. Dutta, S. Banerjee, B. Satpati and S. De, Magnetic field induced electrochemical performance enhancement in reduced graphene oxide anchored Fe3O4 nanoparticle hybrid based supercapacitor, *J. Phys. D Appl. Phys.*, 2018, **51**(37), 375501.

45 V. S. Patil, S. S. Thoravat, S. S. Kundale, T. D. Dongale, P. S. Patil and S. A. Jadhav, Synthesis and testing of polyaniline grafted functional magnetite (Fe3O4) nanoparticles and rGO based nanocomposites for supercapacitor application, *Chem. Phys. Lett.*, 2023, **814**, 140334.

46 T. Prasankumar, B. R. Wiston, C. R. Gautam, R. Ilangovan and S. P. Jose, Synthesis and enhanced electrochemical performance of PANI/Fe3O4 nanocomposite as supercapacitor electrode, *J. Alloys Compd.*, 2018, **757**, 466–475.

47 J. Li, D. Chen and Q. Wu, α-Fe2O3 Based Carbon Composite As Pure Negative Electrode For Application As Supercapacitor, *Eur. J. Inorg. Chem.*, 2019, **2019**(10), 1301–1312.

48 S. S. Raut, L. K. Bommineedi, S. Pande and B. R. Sankapal, Prototype symmetric configured MWCNTs/Fe2O3 based solid-state supercapacitor, *Synth. Met.*, 2021, **271**, 116629.

49 J. Liao, Y. Li, Z. Wang, L. Lv and L. Chang, In-situ preparation of Fe3O4/graphene nanocomposites and their electrochemical performances for supercapacitor, *Mater. Chem. Phys.*, 2021, **258**, 123995.

50 E. Payami, A. Mohammadzadeh, K. D. Safa and R. Teimuri-Mofrad, Ferrocene surface-modified Fe3O4 nanoparticles as prominent electrode material for supercapacitor application, *J. Energy Storage*, 2024, **88**, 111624.

51 H. Song, M. Wu, X. Tang, J. Liang, Y. Zhang, Y. Xie, *et al.*, Synthesis of Fe_3O_4/FeS_2 composites via MOF-templated sulfurization for high-performance hybrid supercapacitors, *J. Alloys Compd.*, 2025, **1010**, 177658.

52 Z. Zhao, W. Zhang, D. Wang, L. Li, Q. Liang, W. Li, *et al.*, Ostwald-Ripening Induced Interfacial Protection Layer Boosts 1,000,000-Cycled Hydronium-Ion Battery, *Angew. Chem., Int. Ed.*, 2024, **63**(50), e202414420.